**Chapter One**

# Computation and visualization of photonic quasicrystal spectra

Steven G. Johnson, Alexander P. McCauley, and Alejandro Rodriguez-Wong

*Department of Applied Mathematics, Massachusetts Institute of Technology,*
*77 Massachusetts Ave.*
*Cambridge, MA 02139, USA*
*stevenj@math.mit.edu*

In this chapter, we describe various approaches to computing the spectra of photonic quasicrystals (PQC). We focus on a recently developed *superspace method* for computing the spectra and eigenstates of PQCs defined by the standard cut-and-project construction, that involves directly solving Maxwell's equations in higher dimensions, where a generalization of Bloch's theorem applies. We emphasize the conceptual and practical differences between superspace and *supercell methods*, which involve computing the eigenfrequencies and/or local density of states to an approximation of the true aperiodic structure.

## 1.1. Introduction and Background

Photonic quasicrystals (PQCs) have a number of unique properties compared to ordinary periodic structures,[1–28] especially in two or three dimensions where they can have greater rotational symmetry and therefore offer some hope of achieving complete photonic band gaps with lower index contrast[8,26,27,29–31] (lower than the roughly 2:1 contrast currently required for periodic structures.[32]). In this chapter, we discuss different approaches to computing the spectra of quasicrystals, emphasizing the relationship between the spectrum computation and the cut-and-project construction of the quasicrystal. We focus on two sets of computational methods, which we denote as either superspace or supercell methods. Until recently, most studies of PQC spectra have been carried out using a variety of *supercell methods*, which involve truncating the PQC in some fashion, e.g. using rational approximants or a large supercell with absorbing/radiating boundary conditions, and computing the spectra of the resulting "supercell" using any number of standard computational techniques. In this way, the aperiodicity of the exact PQC is only approached in the limit in which a large "supercell" calculation captures a sufficiently large portion of the aperiodic lattice. In contrast, the recently-developed *superspace approach*, the main focus of this chapter, involves computing the spectra

---

*Corresponding author

and eigenstates of PQCs defined by the cut-and-project method by directly solving a periodic eigenproblem in a higher-dimensional lattice, where Bloch's theorem applies.[33] The idea that many quasicrystals can be constructed by an irrational slice of a higher-dimensional lattice is well known,[34,35] and in fact is the most common formulation of quasicrystals in two and three dimensions,.[36–38] While the possibility of direct numerical calculations within the higher-dimensional space seems to have been little explored outside of some tight-binding calculations in one-dimensional quantum systems,[39,40] this superspace approach offers a promising route for efficiently computing PQC spectra in general geometries.[33] In what follows, we emphasize the conceptual and practical differences between these two approaches.

In one dimension, a typical quasicrystal is an aperiodic sequence of two or more materials, determined either by a slice of a higher-dimensional lattice[35] or by some "string concatenation" rule,[34] as reviewed by Ref. 28 and also below in Sec. 1.1.1. In either case, the most standard approach to computing the spectra of one-dimensional PQCs involves the application of *supercell methods* in which the PQC is approximated (truncated) using a sufficiently large portion of the aperiodic structure, as reviewed in Sec. 1.1.2. For these one-dimensional systems, efficient $2 \times 2$ transfer-matrix methods are available that allow one to quickly compute the transmission spectra and density of states for supercells consisting of many thousands of layers.[41,42] Two- and three-dimensional quasicrystals are almost always defined as an irrational slice (i.e., incommensurate Miller indices) of a higher-dimensional lattice; for example, the famous Penrose tiling can be viewed as a two-dimensional slice of a five-dimensional cubic lattice or of a four-dimensional root lattice $A_4$.[35] In such cases, supercell computations of a finite portion of the infinite aperiodic structure (or a rational approximate thereof[35,41]) require slower numerical methods, most commonly finite-difference time-domain (FDTD) simulations[6,15,21,43–46] or planewave expansions.[26,47–49] Unfortunately, these methods become very expensive for large supercells, nearly prohibitively so for three-dimensional quasicrystals—there have been experiments for 3D PQCs,[37,38] but as yet few theoretical predictions.[6,50,51] With FDTD methods, for example, the PQC local density of states is typically integrated in Monte-Carlo fashion via random sources or initial conditions,[10,13,25] but many simulations are required to sample all possible modes in a large supercell. Also, the finite domain of a supercell becomes even more significant in higher dimensions where a tractable supercell is necessarily smaller, as there can be localized states[15,19,21,25] whose presence is dependent on the particular region of the PQC considered.

There is also an important distinction between computations that attempt to capture the spectrum of the entire quasicrystal and computations that, by design, calculate only a local density of states in some region or its equivalent, a transmission through a certain slice of the PQC, or related quantities. For example, the local density of states (LDOS) at some point in space, for a given frequency, is proportional to the power radiated by a current source at that point, while the total density of states (giving the full spectrum) is the integral of the LDOS over all space.[52] Computations involving current sources (or external fields) that vary randomly

over a large supercell[3,10,13,25] are essentially performing a Monte-Carlo integration of the LDOS and can therefore be expected to converge to the true density of states. However, calculations that involve sources introduced only in some regions, either to compute the power radiated by those sources or some other sort of transmission measurement[46] are computing a type of LDOS. While the LDOS can be very important in its own right (e.g. to predict spatially varying spontaneous emission rates), it can have dramatic spatial variations that make it an imperfect guide to the overall spectrum. As another example of a suggestive and useful quantity that nevertheless does not necessarily reveal gaps in the overall DOS, several authors have studied transmission through particular finite slices of the QC from a set of incident planewaves.[9,30,31,42,45,53] In such cases, one may observe a low transmission coefficient through a quasicrystal not because of a true gap in the spectrum, but rather because a portion of the spectrum couples poorly to the particular incident field (e.g. because those quasicrystal modes are localized in another region of space, or perhaps simply because of a large field mismatch).

The *superspace method* involves computing the the spectrum of the PQC in the higher-dimensional unit cell defined by its cut-and-project construction. As reviewed in Sec. 1.2, the superspace approach does not require any particular subsection of a large supercell to capture the infinite aperiodic structure—instead, *every* possible supercell of the entire aperiodic structure is uniformly sampled (up to a finite resolution). This involves extending Maxwell's equations to higher dimensions, and computing the resulting spectrum in terms of the Bloch planewave eigenmodes of the higher-dimensional unit cell, which can be discretized using any number of standard numerical grids.[54] In this way, the influence of finite-resolution on the convergence of the spectrum can be systematically understood: one is not "missing" any part of the quasicrystal, so much as resolving the entire quasicrystal with lower resolution. We illustrate this general approach with several example calculations. First, we compare results for a one-dimensional "Fibonacci sequence" with standard one-dimensional transfer-matrix techniques. Second, as mentioned above, we demonstrate how one can use the same technique to study defects in the quasicrystal, as demonstrated in the one-dimensional "Fibonacci" example. We demonstrate the ease with which one can construct and explore different quasicrystals by continuously varying the cut angle, and how exponential convergence with resolution can be obtained from smoothing the superspace structure. We then turn to optimizing the superspace dielectric structure, in order to obtain the largest fractional bandgap, and find that in all cases the optimal structure is actually a *periodic* quarter-wave stack. Finally, we discuss extension of the method to higher-dimensional structures.

### 1.1.1. *Quasicrystals via cut-and-project*

Given a periodic lattice, any lower dimensional cross-section of that lattice may be either periodic or quasi-periodic, depending upon the angle of the cross-section. For example, the periodic 2D cross-sections of a 3D crystal are the lattice planes, defined in crystallography by integer Miller indices. If the Miller indices have irrational ratios, on the other hand, the cross-section is aperiodic but still has long-

range order because of the underlying higher-dimensional periodicity. This is what is known as a "cut-and-project" method of defining a quasicrystalline structure: as a slice of a periodic structure in a higher-dimensional "superspace".[34] (For a thorough discussion of quasicrystals via cut-and-project, see Ref. 34.) Cut-and-project defines a specific class of quasicrystals; equivalently, and more abstractly, cut-and-project corresponds to structures whose Fourier transform has support spanned by a finite number of reciprocal basis vectors (the projection of the reciprocal lattice vectors from higher dimensions).[34,36] This class includes most commonly considered quasicrystals in two or three dimensions, including the Penrose tiling,[35] as well as many one-dimensional quasicrystals including a version of the Fibonacci structure.

For example, consider the Fibonacci PQC in one dimension formed from two materials $\varepsilon_A = 4.84$ and $\varepsilon_B = 2.56$ in layers of thickness $A$ and $B$, respectively, similar to a recent experimental structure.[9] The Fibonacci structure $S$ is then defined by the limit $n \to \infty$ of the string-concatenation rule $S_n = S_{n-2}S_{n-1}$ with starting strings $S_0 = B$ and $S_1 = A$,[9] generating a sequence $BABAABABAABA\cdots$. In the case where $B/A$ is the golden ratio $\tau = (1+\sqrt{5})/2$, exactly the same structure can be generated by a slice of a two-dimensional lattice as depicted in Fig. 1.1..[34] The slice is at an angle $\phi$ with an irrational slope $\tan\phi = 1/\tau$, and the unit cell of the 2D lattice is an $A \times A$ square at an angle $\phi$ in a square lattice with period $(A + B)\sin\phi = a$. Because the slope is irrational, the offset/intercept of the slice is unimportant: any slice at an angle $\phi$ intercepts the unit cell at infinitely many points, filling it densely.
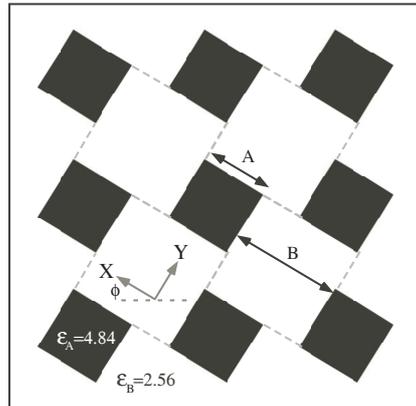


**Figure 1.1.**   Unit cell of the Fibonacci superspace dielectric. The physical dielectric is obtained by taking a slice at an angle $\tan\phi = \tau$. Black/white are the dielectric constants of the structure factor material and air, chosen to be $\varepsilon = 4.84$ and $\varepsilon = 2.56$, respectively.

For thickness ratios $B/A \neq \tau$, the Fibonacci structure cannot be constructed by cut-and-project, and in general string-concatenation rules can produce a different range of structures (such as the Thue-Morse PQC[55]) than cut-and-project.[a] This is

---

[a]Similarly, there are two-dimensional structures defined by analogous rules that cannot be formed by cut-and-project, and some structures such as the 2D Fibonacci crystal where it is unclear whether a cut-and-project construction is possible.[56,57]

partly a question of definition—some authors reserve the term "quasicrystal" for cut-and-project structures.[35] In any case, cut-and-project includes a wide variety of aperiodic structures, including most of the structures that have been proposed in two or three dimensions (where they can be designed to have $n$-fold rotational symmetry for any $n$), and are the class of quasicrystals that we consider in this paper.

In general, let $d \leq 3$ be the number of physical dimensions of a quasicrystal structure generated by a $d$-dimensional "slice" of an $n$-dimensional periodic structure ($n > d$). Denote this slice by $X$ (the physical space) with coordinates $\mathbf{x} \in \mathbb{R}^d$, and denote the remaining $n - d$ coordinates by $\mathbf{y} \in \mathbb{R}^{n-d}$ in the "unphysical" space $Y$ (so that the total $n$-dimensional superspace is $Z = X \oplus Y$). The primitive lattice vectors $\mathbf{R}_i \in Z$ define the orientation of the lattice with respect to the slice (rather than vice versa), with corresponding primitive reciprocal vectors $\mathbf{G}_i$ defined by the usual $\mathbf{R}_i \cdot \mathbf{G}_j = 2\pi\delta_{ij}$.[34] (The concept of an "irrational slice" is commonly used in the quasicrystal literature. However, a general definition of what is meant by an "irrational slice" seems difficult to find, and less evident in dimensions $d > 2$. A more precise definition of "irrational slice" in general dimensions is given in Ref. 33.

The physical dielectric function $\varepsilon(\mathbf{x})$ is then constructed by starting with a periodic dielectric function $\varepsilon(\mathbf{x}, \mathbf{y})$ in the superspace and evaluating it at a fixed $\mathbf{y}$ (forming the slice). Because an irrational slice is dense in the unit cell of the superspace,[34] it doesn't matter what value of $\mathbf{y}$ one chooses, as discussed below. In principle, one could define the unit cell of $\varepsilon$ in the superspace to be any arbitrary $n$-dimensional function, but in practice it is common to "decorate" the higher-dimension unit cell with extrusions of familiar $d$-dimensional objects.[34,35] More precisely, "cut-and-project" commonly refers to constructions where a set of lattice points within a finite window of the cut plane are projected onto the cut plane, and this is equivalent to a simple cut where objects at the lattice points are extruded in the $y$ direction by the window width.[34] In particular, the extrusion window is commonly an inverted projection (shadow) of the unit cell onto the $y$ directions,[34] although this is not the case for the Fibonacci construction of Fig. 1.1..

Note that the higher-dimensional lattice need not be hypercubic. For example, the Penrose tiling can be expressed as a two-dimensional slice of either a five-dimensional hypercubic lattice or of a non-orthogonal four-dimensional root lattice $A_4$.[35] For computational purposes, the lower the dimensionality the better.

### 1.1.2. *Supercell approach*

As mentioned above, aside from the superspace approach, the most common approach to computing PQC spectra is the supercell method, which we briefly describe here. For convenience we examine this method using an example structure known as the Fibonacci quasicrystal. In the supercell approach, the exact quasicrystal is replaced with a *rational approximate*, in which the structure of Fig. 1.1. is constructed from a cut angle of $\tan\phi = \frac{p}{q}$, where $\frac{p}{q}$ is a rational number close to $\tau$. For example, the first few rational approximates to $\tau$ are $1/1, 2/1, 3/2, 5/3 \dots$. As the cut line has a rational slope, the cut-and-project construction will yield a
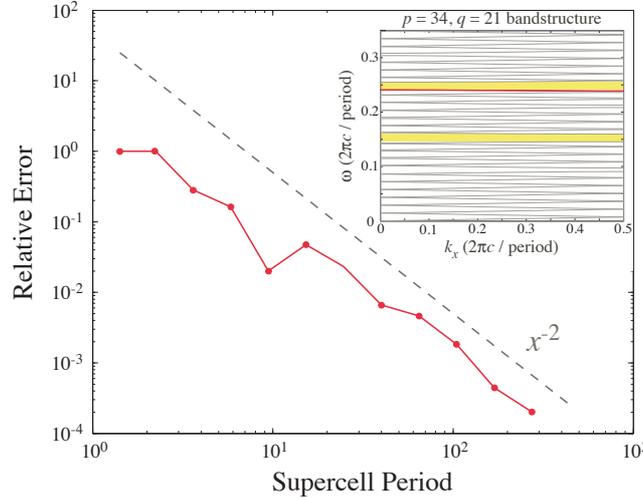
**Figure 1.2.**   Error in the lower band edge of the Fibonacci PQC defined by the cut-and-project method applied to the structure in Fig. 1.1., as a function of the supercell period, which is $\sqrt{p^2 + q^2}$, where $p/q$ is a rational approximate to $\tau = \frac{1+\sqrt{5}}{2}$. The dashed black line indicates quadratic convergence, consistent with the fact that $|p/q - \tau| \sim \frac{1}{p^2+q^2}$. Inset: bandstructure for the $p = 34$, $q = 21$ approximate. The $k_x = 0$ point of the red band indicates the frequency points used for the convergence.

periodic structure with period $\sqrt{p^2 + q^2}$. As $p$ and $q$ increase, the period of the structure diverges, while the error $\left| \frac{p}{q} - \tau \right|$ goes to zero. These successively larger periodic structures therefore approximate the exact aperiodic structure. To examine how rapidly the bandstructure of these rational approximates converges to the exact bandstructure, we examine the lower band edge of a bandgap at $\omega \approx 0.235$ for the Fibonacci PQC described in above (Fig. 1.1.), shown in the inset to Fig. 1.2.. Fixing the Bloch vector of the periodic structure to be $k_x = 0$, we plot the error of this band edge for successive rational approximates in the main part of Fig. 1.2.. Although the convergence isn't exact, the error generally goes as the inverse square of the structure period.

This dependence can be understood from the convergence of the rational approximates $p/q$ to $\tau$: for any real number $x$, the error in the rational approximate is bounded by $\left| \frac{p}{q} - x \right| < \frac{1}{\sqrt{5}q^2}$.[58] Since $p \sim q$, this bound goes as the inverse-square of the period (although some irrational numbers may have rational approximants that converge faster, depending on their continued-fraction expansions[59]). However, in Sec. 1.3.4 we will see that the superspace method can yield *exponential* convergence in the bandstructure for a smoothed version of Fig. 1.1., regardless of the value of $\phi$.

## 1.2.   Computations in Higher Dimensions

Although the cut-and-project technique is a standard way to *define* the quasicrystal structure, most computational studies of photonic quasicrystals simulate the resulting structure only in the projected ($d$-dimensional) physical space (the supercell approach). In the superspace approach, however, one instead extends Maxwell's equations into the periodic $n$-dimensional superspace, where Bloch's theorem applies. By looking at only the unit cell in $n$ dimensions one can capture the infinite $d$-dimensional quasicrystal.

Let us start with Maxwell's equations in the physical space $X$ for the quasicrystal $\varepsilon(\mathbf{x}, \mathbf{y})$ at some fixed $\mathbf{y}$ (that is, $\mathbf{y}$ is viewed as a parameter, not a coordinate). Maxwell's equations can be written as an eigenproblem for the harmonic modes $\mathbf{H}(\mathbf{x}, \mathbf{y})e^{-i\omega t}$,[60] where again $\mathbf{y}$ appears as a parameter.

$$\nabla_{\mathbf{x}} \times \frac{1}{\varepsilon(\mathbf{x}, \mathbf{y})} \nabla_{\mathbf{x}} \times \mathbf{H} = (\omega/c)^2 \mathbf{H} \tag{1.1}$$

where $\nabla_{\mathbf{x}} \times$ denotes the curl with respect to the $\mathbf{x}$ coordinates. Assuming that the structure is quasicrystalline, i.e. that $X$ is an irrational slice of the periodic superspace $Z$, then $\omega$ should not depend upon $\mathbf{y}$.[39] The reason is that $\mathbf{y}$ only determines the offset of the "initial" slice of the unit cell (for $\mathbf{x} = 0$), but as we reviewed above the slice (considered in all copies of the unit cell) fills the unit cell densely. Therefore, any change of $\mathbf{y}$ can be undone, to arbitrary accuracy, merely by offsetting $\mathbf{x}$ to a different copy of the unit cell. An offset of $\mathbf{x}$ doesn't change the eigenvalues $\omega$, although of course it offsets the eigenfunctions $\mathbf{H}$.

The fact that $\omega$ is independent of $\mathbf{y}$ allows us to re-interpret Eq. (1.1), without actually changing anything: we can think of $\mathbf{y}$ as a coordinate rather than a parameter, and the operator on the left-hand side as an operator in $d$-dimensional space. Note that $\mathbf{H}$ is still a three-component vector field, and $\nabla_{\mathbf{x}} \times$ is still the ordinary curl operator along the $\mathbf{x}$ directions, so this is not so much a higher-dimensional version of Maxwell's equations as an extension of the unmodified ordinary Maxwell's equations into a higher-dimensional parameter space. The $\mathbf{y}$ coordinate appears in the operator only through $\varepsilon$. Because $\omega$ is independent of $\mathbf{y}$, i.e. it is just a number rather than a function of the coordinates, Eq. (1.1) in higher dimensions is still an eigenproblem, and its spectrum of eigenvalues $\omega$ is the same as the spectrum of the $d$-dimensional quasicrystal, since the equations are identical. The physical solution is obtained by evaluating these higher-dimensional solutions at a fixed $\mathbf{y}$, say $\mathbf{y} = 0$ (where a different $\mathbf{y}$ merely corresponds to an offset in $\mathbf{x}$ as described above).

For a real, positive $\varepsilon$, both the physical operator and the extended operator in in Eq. (1.1) are Hermitian and positive semi-definite, leading to many important properties such as real frequencies $\omega$.[60]

### 1.2.1.   *Bloch's theorem and numerics for quasicrystals*

Because the superspace eigenproblem is periodic, Bloch's theorem applies: the eigenfunctions $\mathbf{H}(\mathbf{x}, \mathbf{y})$ can be written in the Bloch form $\mathbf{h}(\mathbf{z})e^{i\mathbf{k}\cdot\mathbf{z}}$, where $\mathbf{h}$ is a

*periodic* function defined by its values in the unit cell, and $\mathbf{k}$ is the $n$-dimensional Bloch wavevector.[60]

Here, $\mathbf{k}$ determines the phase relationship between $\mathbf{H}$ in different unit cells of the superspace, but it does not have a simple interpretation once the solution is projected into physical space. The reason is that $\mathbf{h}$, viewed as a function of $\mathbf{x}$, is again only quasiperiodic: translation in $\mathbf{x}$ "wraps" the slice into a different portion of the unit cell, so both $\mathbf{h}$ and $e^{i\mathbf{k}\cdot\mathbf{z}}$ change simultaneously and the latter phase cannot be easily distinguished. This prevents one from defining a useful phase or group velocity of the PQC modes.

The key point is that Bloch's theorem reduces the eigenproblem to a finite domain (the $n$-dimensional unit cell), rather than the infinite domain required to describe the quasicrystal solutions in physical space. This means that standard numerical methods to find the eigenvalues of differential operators are immediately applicable. For example, since the solution $\mathbf{h}$ is periodic, one can apply a planewave expansion method[61] for $\mathbf{h}$:

$$\mathbf{h}(\mathbf{z}) = \sum_{\mathbf{G}} \tilde{\mathbf{h}}_{\mathbf{G}} e^{i\mathbf{G}\cdot\mathbf{z}}, \tag{1.2}$$

where the summation is over all $n$-dimensional reciprocal lattice vectors $\mathbf{G}$. Because the curl operations only refer to the $\mathbf{x}$ coordinates, $\nabla_{\mathbf{x}} \times \mathbf{h}$ is replaced by a summation over $\mathbf{g}_{\mathbf{x}} \times \tilde{\mathbf{h}}_{\mathbf{G}}$, where $\mathbf{g}_{\mathbf{x}}$ denotes $\mathbf{G}$ projected into $X$. The resulting eigenproblem for the Fourier coefficients $\tilde{\mathbf{h}}$ (once they are truncated to some wavevector cutoff) can be computed either by direct dense-matrix methods[62] or, more efficiently, by iterative methods exploiting fast Fourier transforms.[61] In the present paper, we do the former, which is easy to implement in higher dimensions. We should also remind the reader that there is a constraint $\nabla_{\mathbf{x}} \cdot \mathbf{H} = 0$ on the eigenfunctions, in order to exclude unphysical solutions with static magnetic charges. In a planewave method, this leads to a trivial constraint $(\mathbf{k}_{\mathbf{x}} + \mathbf{g}_{\mathbf{x}}) \cdot \tilde{\mathbf{h}} = 0$, again with $\mathbf{k}$ and $\mathbf{G}$ projected into $X$.

### 1.2.2. *The spectrum of the quasicrystal*

With a familiar eigenproblem arising from Bloch's theorem, such as that of a periodic physical structure, the eigenvalues form a band structure: discrete bands $\omega_n(\mathbf{k})$ that are continuous functions of $\mathbf{k}$, with a finite number of bands in any given frequency range.[63] For a finite-resolution calculation, one obtains a finite number of these bands $\omega_n$ with some accuracy that increases with resolution, but even at low resolutions the basic structure of the low-frequency bands is readily apparent. The eigenvalues of the higher-dimensional quasicrystal operator of Eq. (1.1), on the other hand, are quite different.

The underlying mathematical reason for the discrete bandstructure of a physical periodic structure is that the Bloch eigen-operator for a periodic physical lattice, $(\nabla + i\mathbf{k}) \times \frac{1}{\varepsilon}(\nabla + i\mathbf{k}) \times$, is the inverse of a compact integral operator corresponding to the Green's function, and hence the spectral theorem applies.[64] Among other things, this implies that the eigenvalues at any given $\mathbf{k}$ for a finite unit cell form a discrete increasing sequence, with a finite number of eigenvalues below any finite $\omega$. The same nice property does not hold for the operator extended to

$n$ dimensions, because along the **y** directions we have no derivatives, only a variation of the scalar function $\varepsilon$. Intuitively, this means that the fields can oscillate very fast along the **y** directions without necessarily increasing $\omega$, allowing one to have infinitely many eigenfunctions in a finite bandwidth. More mathematically, an identity operator is not compact and does not satisfy the spectral theorem,[64] and since the operator of Eq. (1.1) is locally the identity along the **y** directions the same conclusion applies. This means that, when the **y** direction is included as a coordinate, it is possible to get an infinite number of bands in a finite bandwidth at a fixed **k**.

In fact, as we shall see below, this is precisely what happens, and moreover it is what *must* happen in order to reproduce the well-known properties of quasicrystal spectra. It has been shown that quasicrystal spectra can exhibit a fractal structure,[34] with infinitely many gaps (of decreasing size) in a finite bandwidth, and such a structure could not arise from an ordinary band diagram with a finite number of bands in a given bandwidth. Of course, once the unit cell is discretized for numerical computation, the number of degrees of freedom and hence the number of eigenvalues is finite. However, as the resolution is increased, not only do the maximum frequency and the accuracy increase as for an ordinary computation, but also the number of bands in a given bandwidth increases. Thus, as the resolution is increased, more and more of the fractal structure of the spectrum is revealed.

## 1.3. One-dimensional results

As a proof of concept implementation of cut-and-project, we construct a Fibonacci quasicrystal in Sec. 1.3.1 using the projection method described above, compute the bandstructure as a function of the projected wave-vector $k_d$ and compare to a transfer-matrix calculation of the same quasicrystal structure. We also demonstrate the field visualization enabled by the projection method, both in the superspace ($n$ dimensions) as well as in the physical space ($d$ dimensions). In Sec. 1.3.2, we demonstrate how this method can accommodate systems with defects. Finally, we explore several one-dimensional quasicrystal configurations in Sec. 1.3.3 by varying the cut angle $\phi$.

### 1.3.1. *Fibonacci quasicrystal*

#### 1.3.1.1. *Spectrum*

We solved Eq. (1.1) numerically using a planewave expansion in the unit cell of the 2D superspace, as described above, for the 1D Fibonacci quasicrystal structure depicted in Fig. 1.1.. The resulting band diagram is shown in Fig. 1.3.(left), along with a side-by-side comparison of the local density of states in Fig. 1.3.(right) calculated using a transfer-matrix approach with a supercell of $10^4$ layers.[65] The two calculations show excellent agreement in the location of the gaps, except for one or two easily-identified spurious bands inside some of the gaps, which are discussed in further detail below. The most important feature of Fig. 1.3.(left) is the large number of bands even in the finite bandwidth $\omega \in [0, 0.4]$, with the num-
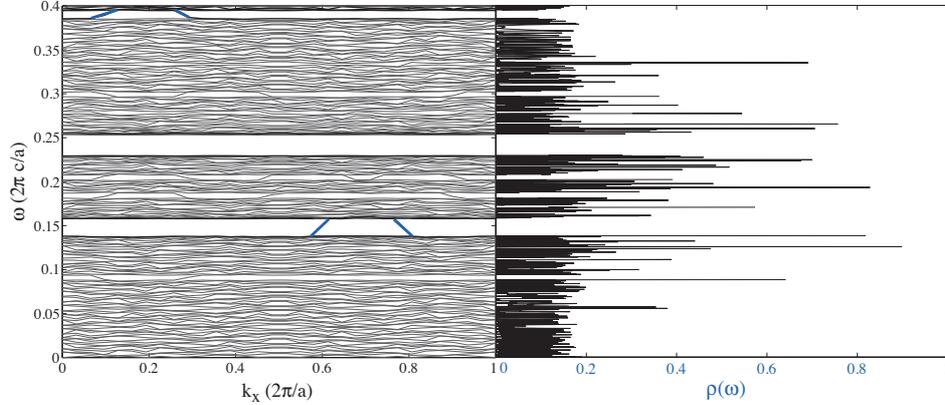
**Figure 1.3.**   *Left:* Frequency spectrum $\omega$ of the Fibonacci quasicrystal vs. "wave-vector" $k_x$. The blue lines indicate spurious states which arise due to finite resolution effects (see text). *Right:* Corresponding density of states $\rho(\omega)$ computed using a transfer-matrix technique with a supercell of $10^4$ layers.
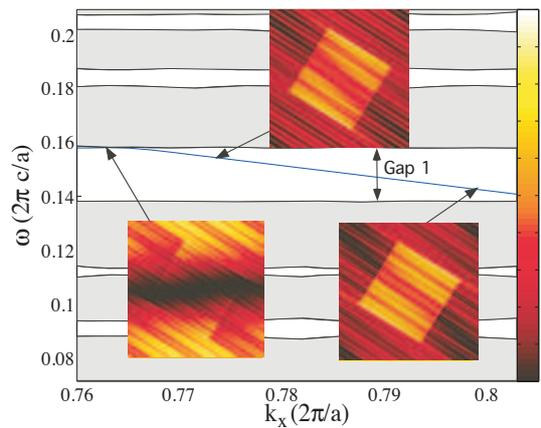


**Figure 1.4.**   Enlarged view of the Fibonacci spectrum showing a gap with a spurious band crossing it. Insets show the magnetic field $|H_z|$ for the spurious band at various $k_x$—the localization of this mode around the $X$-parallel edges of the dielectric indicate that this is a discretization artifact.

ber of bands increasing proportional to the spatial resolution (planewave cutoff). This is precisely the feature predicted abstractly above, in Sec. 1.2.2: at a low resolution, one sees only the largest gaps, and at higher resolutions further details of the fractal spectrum are revealed as more and more bands appear within a given bandwidth, very different from calculations for periodic physical media. The important physical quantity is not so much the band structure, since **k** has no simple physical meaning as discussed previously, but rather the density of states formed by projecting the bandstructure onto the $\omega$ axis. In this density of states, the small number of spurious bands within the gaps, which arise from the discretization as discussed below, plays no significant role: the density of states is dominated by the

huge number of flat bands (going to infinity as the resolution is increased), and the addition of one or two spurious bands is negligible.

### 1.3.1.2. *Spurious modes*

As the wavevector **k** varies, most of the bands in the spectrum of Fig. 1.3. are flat, except for certain modes (highlighted in blue) which appear to cross the band gaps relatively quickly. In fact, a simple argument shows that, in the limit of infinite resolution, the physical spectrum cannot depend on **k**, and hence any strongly **k**-dependent band must be a numerical artifact. First, $\omega$ cannot depend on the components of **k** in the unphysical directions $Y$, because the Maxwell operator of Eq. (1.1) has no **y**-derivatives (equivalently, any phase oscillations in **y** commute with the operator). Second, $\omega$ cannot depend on the components of **k** in the physical directions $X$, either. The reason is that, from Bloch's theorem, **k** and **k** + **G** give the same eigensolutions for any reciprocal lattice vector **G**, and the projections of the reciprocal lattice vectors are dense in $X$ for a quasicrystal.

These "spurious" bands that appear arise from the discretization of the dielectric interfaces parallel to the slice direction. Because the slice is at an irrational angle, it will never align precisely with a uniform grid, resulting in inevitable staircasing effects at the boundary. With ordinary electromagnetic simulations, these staircasing effects can degrade the accuracy,[66] but here the lack of derivatives perpendicular to the slice allows spurious modes to appear along these staircased edges (there is no frequency penalty to being localized perpendicular to the slice). Indeed, if one looks at the field patterns for the spurious modes, one of which is shown in the inset of Fig. 1.3.(right), one sees that the field intensity is peaked along the slice-parallel dielectric interfaces. Because they are localized to these interfaces and are therefore dominated by the unphysical staircasing, the spurious modes behave quite differently from the "real" solutions and are easily distinguished qualitatively and quantitatively (e.g via their **k**-dependence). In one dimension, as the resolution is increased, the number of spurious modes in a given gap does not increase like all of the other bands, because the thickness of the staircased interface region decreases proportional to the resolution. This makes the gaps in the band-structure obvious: here, they are the only frequency ranges for which the number of eigenvalues does not increase with resolution. Equivalently, as noted above, the contribution of the spurious bands to the density of states is asymptotically negligible as resolution is increased. However, in higher dimensions we have found that the presence of spurious modes is more pronounced and tends to obscure even the large bandgaps. Therefore, we desire a rigorous method to identify and eliminate spurious modes, which we now describe.

Examining the right panel of Fig. 1.5., which contains the frequency spectrum of the same Fibonacci lattice explored previously, we see that the dispersion curves of certain spurious in different bandgaps appear to fall along a straight line (the black dashed line in Fig. 1.5.[right]). This dispersion curve is characteristic of modes in a uniform medium. This observation lead us to speculate that spurious modes appear at the boundaries of the reciprocal space, that is, at the extremal values of **k** + **G** allowed in the computational cell. As they are at the cell boundaries, these
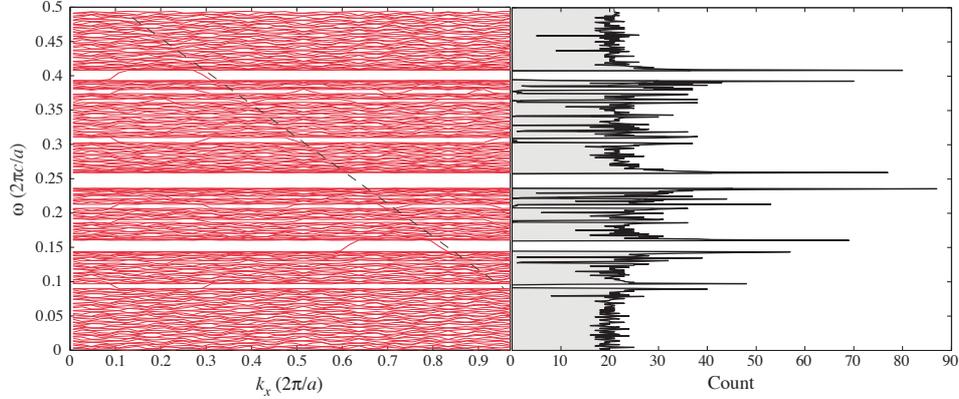
**Figure 1.5.**   Identification and removal of spurious modes in one dimension. Left: spectrum of the Fibonacci quasicrystal, as in Fig. 1.3.. We have superposed a black dashed line to indicate that the spurious modes appear to largely follow a linear dispersion relation. Right: density-of-states computed by removing all modes that satisfy $\lambda(\mathbf{H}) \geq 0.9$, where $\lambda$ is defined in Eq. (1.3). All spurious modes in the large bandgaps have vanished.

modes are not represented accurately because their coupling to nearby values of $\mathbf{k} + \mathbf{G}$ are not accounted for. In normal planewave-expansion methods, this does not matter as one is usually interested in the low-frequency modes, which are not strongly affected by the truncation at high values of $\mathbf{k} + \mathbf{G}$. However, in this case high values of $|\mathbf{k} + \mathbf{G}|$ can correspond to low values of $|(\mathbf{k} + \mathbf{G})_{\mathbf{x}}|$ - therefore, this truncation may manifest itself even in the low-lying spectrum. Testing this hypothesis, we filtered the frequency spectrum of Fig. 1.5.(Left) using the following measure

$$\lambda(\mathbf{H}) \equiv \frac{\sum_{\mathbf{G} \in \text{Extreme}} |\mathbf{H_G}|^2}{\sum_{\mathbf{G}} |\mathbf{H_G}|^2} . \tag{1.3}$$

Here a reciprocal vector is "extreme" if it is at the boundary of the computational cell. If $\lambda(\mathbf{H}) > 0.9$, we exclude the mode. The filtered results are shown in Fig. 1.5.(Right). We depict the results as a density of states because the bands now discontinuously jump across the bandgaps as $k_x$ is varied. Shown in this way, we see that all spurious modes in the large bandgaps have been removed, validating our assumptions.

We can directly examine the behavior of spurious modes by examining the $\mathbf{H_G}$ directly in reciprocal space. These are shown in Fig. 1.6. and Fig. 1.7.. The former depicts a spurious mode in the main bandgap, while the latter depicts a "physical" mode. There is a clear difference between the two modes, with the spurious mode

strongly weighted at the cell boundary (in this case, the weight is over 99% on the boundary).
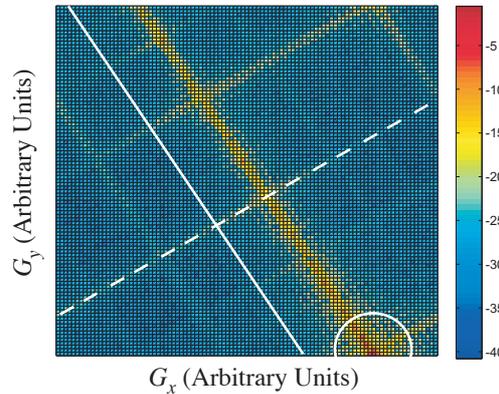


**Figure 1.6.** Fourier-space spectrum $|\mathbf{H_G}|^2$ of a spurious mode, on a log scale: dashed white line denotes the "physical" $X$ direction in which fluctuations carry an energy penalty, and the solid white line denotes the "un-physical" $Y$ direction. Circle denotes the peak in the mode's Fourier-space support, which occurs at the boundary of the computational cell.
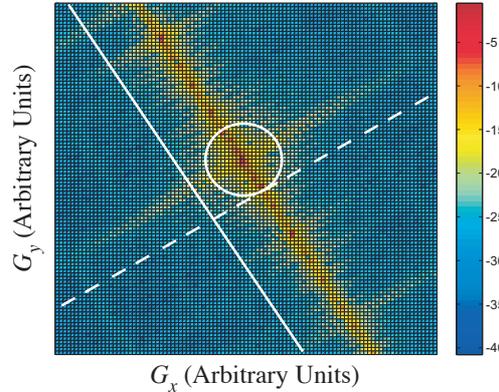


**Figure 1.7.** Fourier-space spectrum $|\mathbf{H_G}|^2$ of a physical mode, on a log scale. In contrast to Fig. 1.6., the primary support of this mode occurs in the center of the computational cell.

### 1.3.1.3. *Visualizing the eigenmodes in superspace*

Computing the eigenmodes in the higher-dimensional superspace immediately suggests a visualization technique: instead of plotting the quasiperiodic fields as a function of the physical coordinates $x$ by taking a slice, plot them in the two-dimensional superspace. This has the advantage of revealing the entire infinite aperiodic field pattern in a single finite plot.[39] Such plots were already used above, to aid in understanding the spurious modes localized at staircased interfaces. A typical extended mode profile is shown in Fig. 1.8., plotted both as a function of
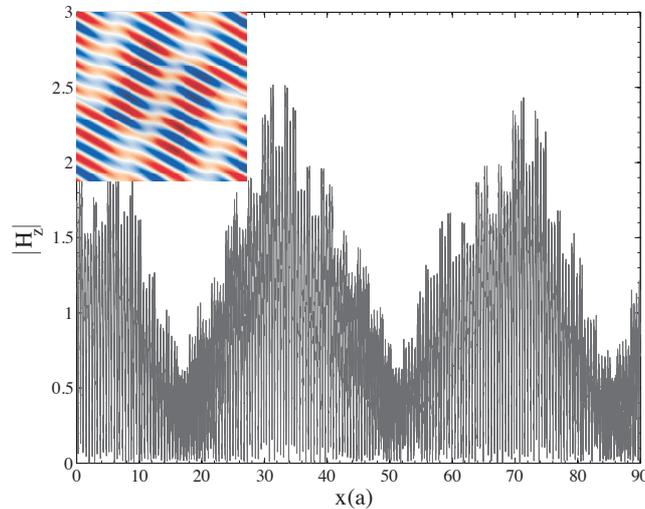
**Figure 1.8.** Plot of the magnetic field amplitude $|H_z|$ for a band-edge state taken along a slice of the two-dimensional superspace (in the $\phi$ direction). *Inset:* Two-dimensional superspace field profile (red/white/blue indicates positive/zero/negative amplitude).

the physical coordinate $x$ for large supercell and also in the unit cell of the superspace (inset). In the inset superspace plot, one can clearly see the predicted field oscillations perpendicular to the slice plane, as well as a slower oscillation rate (inversely proportional to the frequency) parallel to the slice. In the plot versus $x$, one can see the longer-range quasi-periodic structure that arises from how the slice wraps around the unit cell in the superspace. The factor of three to four long-range variations in the field amplitude are suggestive of the critically localized states (power-law decay) that one expects to see in such quasicrystals.[9,67,68]

By visualizing the bands in this way, we can demonstrate the origin of the quasicrystal band gap in an interesting way. In an ordinary photonic crystal, the gap arises because the lowest band concentrates its electric-field energy in the high-dielectric regions (due to the variational principle), while the next band (above the gap) is forced to have a nodal plane in these regions (due to orthogonality).[60] A very similar phenomenon can be observed in the quasicrystal eigenmodes, when plotted in the superspace. In particular, Fig. 1.9. displays the electric-field energy distribution of the band-edge states just above and below gaps 1 and 2 of Fig. 1.3.. Very similar to an ordinary two-dimensional photonic crystal, the bands just below the gaps are peaked in the dielectric squares, whereas the upper-edge bands have a nodal plane in these squares. If the same fields were plotted only in the physical coordinate space, the position of the peaks and nodes would vary between adjacent layers and this global pattern (including the relationship between the two gaps) might not be apparent. In contrast to a two-dimensional photonic crystal, on the other hand, the quasicrystalline field pattern has fractal oscillations in the superspace.
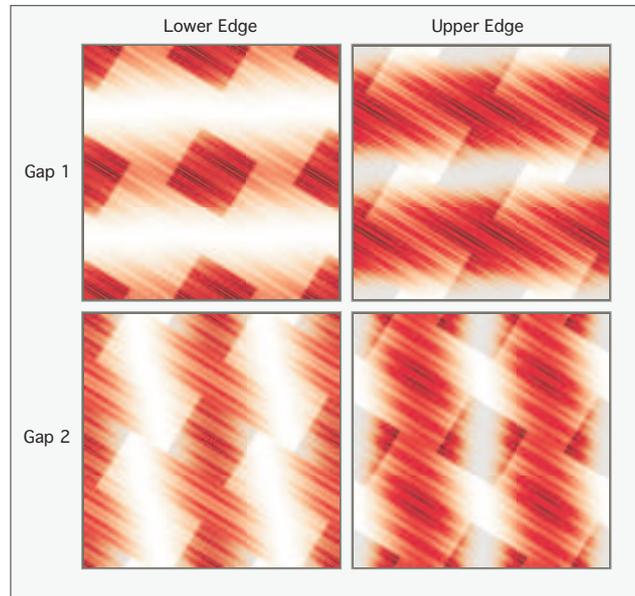
**Figure 1.9.** Electric field energy distribution of the band edge states of gaps 1 and 2 in Fig. 1.3.. Although they have a complex small-scale structure, the large-scale variation is easily understood in terms of the structure of the superspace.
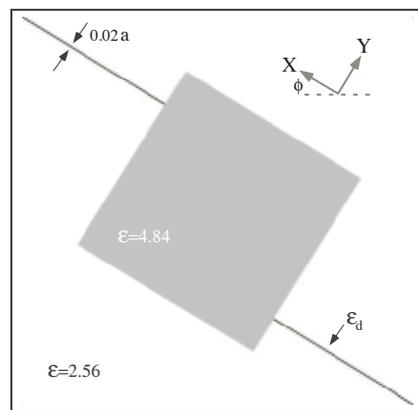


**Figure 1.10.** Dielectric for the Fibonacci chain with $\varepsilon = 2.56$ (light blue), and a defect—an additional $\varepsilon_d = 8.0$ layer, shown in gray.

### 1.3.2. *Defect modes*

Much of the interest in quasicrystal band gaps, similar to the analogous case of band gaps in periodic structures, centers around the possibility of localized states: by introducing a defect in the structure, e.g. by changing the thickness of a single layer, one can create exponentially localized states in the gap.[4,69] In periodic systems, because such defects break the periodicity, they necessitate a larger computational cell, or supercell, that contains many unit cells. In quasicrystal systems

once the gaps are known, on the other hand, defect states are arguably *easier* to compute than the gaps of the infinite structure, because an exponentially localized defect mode can be computed accurately with a traditional supercell and the infinite quasicrystal per se need not be included. Nevertheless, the superspace approach allows one to compute defect modes using the same higher-dimensional unit cell, which demonstrates the flexibility of this approach and provides an interesting (but not obviously superior) alternative to traditional supercells for defect states.

Ideally, if one had infinite spatial resolution, a defect in the crystal would be introduced as a very thin perturbation parallel to the slice direction. As the thickness of this perturbation goes to zero, it intersects the physical slice at greater and greater intervals in the physical space, corresponding to localized defects that are separated by arbitrarily large distances. In practice, of course, the thickness of the perturbation is limited by the spatial resolution, but one can still obtain defects that are very widely separated—since the associated defect modes are exponentially localized, the coupling between the defects is negligible. In other words, one effectively has a very large supercell calculation, but expressed in only the unit cell of the higher-dimensional lattice.
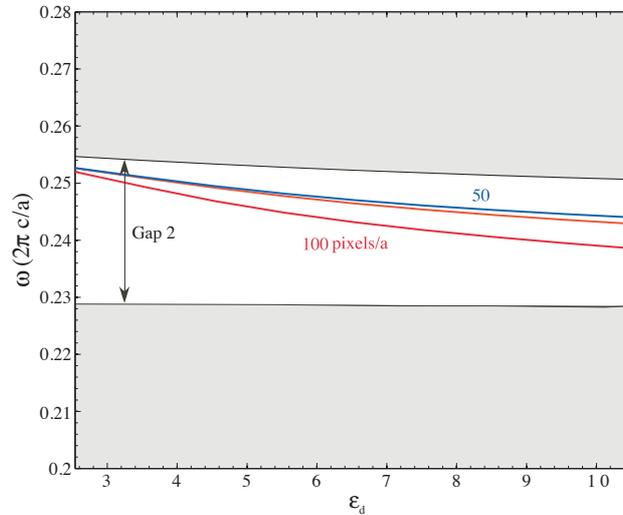


**Figure 1.11.** Varying the defect epsilon for resolutions 50 (blue) and 100 (red). The thickness of the defect is fixed to 0.02 lattice constants. The number of spurious modes increases with the resolution, the true defect state being the lowest of these modes.

As an example, we changed an $\varepsilon = 2.56$ layer to $\varepsilon = \varepsilon_d$ at one place in the Fibonacci quasicrystal. The corresponding superspace dielectric function is shown in Fig. 1.10., where the defect is introduced as a thin (0.02$a$) strip of $\varepsilon_d$ parallel to the slice direction. We compute the bandstructure as a function of the defect dielectric constant $\varepsilon_d$, varying it from the normal dielectric $\varepsilon_d = 2.56$ up to $\varepsilon_d = 11$. The thickness of the defect in the unphysical direction was fixed to be $\approx 0.02$. The resulting eigenvalues as a function of $\varepsilon_d$ are shown in Fig. 1.11. for two different

(a)                                         (b)
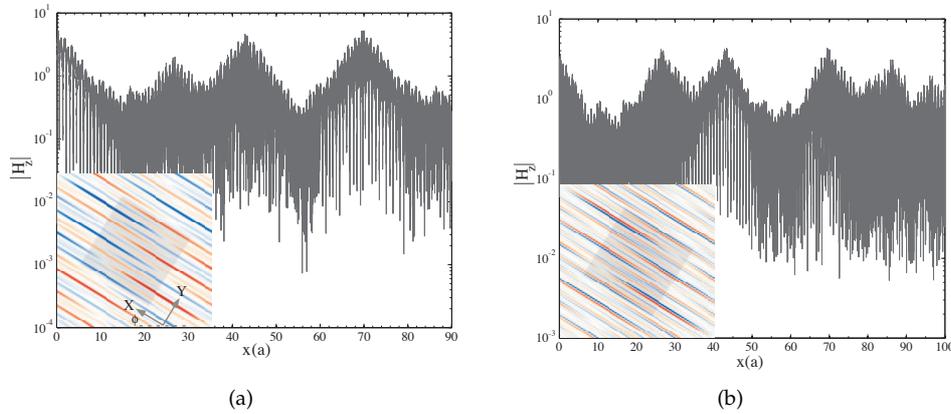
**Figure 1.12.**   Semi-log plots of the magnetic field magnitude $H_z$ for the lowest (a) and highest (b) defect state for the configuration shown in Fig. 1.10.. *Insets:* Two-dimensional superspace visualizations of the defect states.  Note the additional node in the lower figure (corresponding to an unphysical oscillation).

spatial resolutions of 50 (blue) and 100 (red) pixels/$a$. When the resolution is 50 the defect is only one pixel thick, the discretization effects might be expected to be large, although the frequency is within about 2% of the higher-resolution calculation. At the higher resolution, the frequency of the mode is converging (it is within 0.3% of a resolution-200 calculation, not shown). However, at the higher resolution there is a second, spurious mode due to the finite thickness (2 pixels) of the defect layer—this spurious mode is easily identified when the field is plotted Fig. 1.12.(bottom), because it has a sign oscillation perpendicular to the slice (which would be disallowed if we could make the slice infinitesimally thin).

The defect modes for the resolution 100 are plotted in Fig. 1.12. for both the real and the spurious modes, versus the physical coordinate ($x$) and also in the superspace unit cell (insets). When plotted versus the physical coordinate $x$ on a semilog scale, we see that the modes are exponentially localized as expected. The defect mode appears at multiple $x$ values (every $\sim 20a$ on average) because the defect has a finite thickness—the physical slice intersects it infinitely many times (quasiperiodically), as discussed above. The spurious mode (bottom panel) is also exponentially localized; it has a sign oscillation perpendicular to the slice direction (inset) which causes it to have additional phase differences between the different defects.

Nevertheless, as noted above, one may argue that the main advantages of the superspace approach lie in its ability to capture the gaps and modes of the infinite, defect-free quasicrystal, rather than the properties of localized defect modes.

### 1.3.3.  *Continuously varying the cut angle*

The cut-and-project construction of quasicrystals provides a natural way to parameterize a family of periodic and quasiperiodic structures, via the cut angle $\phi$. It is
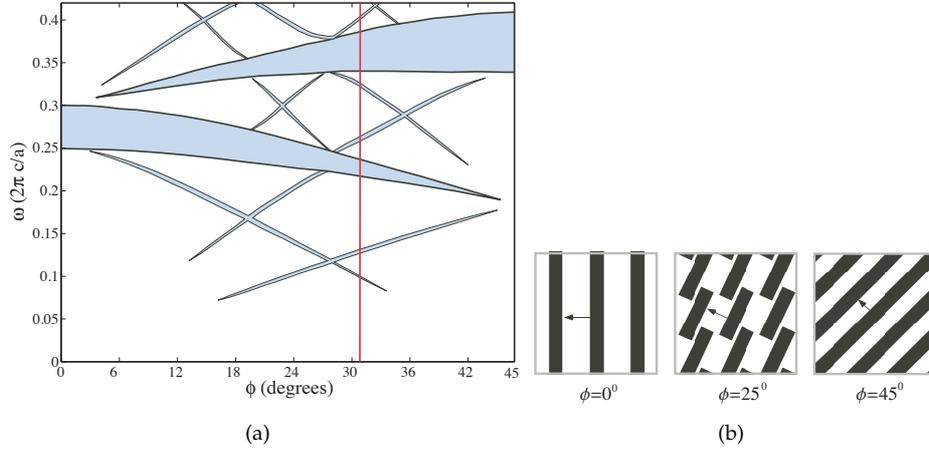
**Figure 1.13.**   Projected bandstructure vs. cut angle $\phi$, showing different one-dimensional quasicrystal realizations. The vertical red line indicates the spectrum when the slope is the golden ratio $\tau$ (the spectra of $\phi$ and $\pi - \phi$ are equivalent)

interesting to observe how the spectrum and gaps then vary with $\phi$.

As $\phi$ is varied continuously from $0°$ to $45°$, the structures vary from period $a$ to quasi-periodic lattices (for $\tan\phi$ irrational) to long-period structures ($\tan\phi$ rational with a large denominator) to a period $a\sqrt{2}$ crystal. As we change $\phi$, we rotate the objects in the unit cell, so that they are always extruded along the $y$ direction with a length equal to the projection of the unit cell onto $y$ [$a(\sin\phi + \cos\phi)$], correspond-ing the usual cut-and-project construction.[34] In this case, the spectrum varies con-tinuously with $\phi$, where the rational $\tan\phi$ correspond to "rational approximates" of the nearby irrational $\tan\phi$.[36,70] For a general unit cell with a rational $\tan\phi$, the physical spectrum might depend on the slice offset **y** and hence different from the total superspace spectrum, but this is not the case for dielectric structures like the one here, which satisfy a "closeness" condition[70] (the edges of the dielectric rods overlap when projected onto the $Y$ direction). This makes the structure **y**-independent even for rational slices.[70] The resulting structures are shown in the bottom panel of Fig. 1.13. for three values of $\phi$.

The corresponding photonic band gaps are shown in the top panel of Fig. 1.13., as a continuous function of $\phi$. Only the largest gaps are shown, of course, since we are unable to resolve the fractal structure to arbitrary resolution. As might be expected, there are isolated large gaps at $\phi = 0°$ and $\phi = 45°$ corresponding to the simple $ABAB\cdots$ periodic structures at those angles (with period $a$ and $a/\sqrt{2}$, respectively, the latter resulting from two layers per unit cell). The $\phi = 45°$ gap is at a higher frequency because of its shorter period, but interestingly it is not continuously connected to the $\phi = 0°$ gap.

The reason for this is that the two gaps are dominated by different superspace reciprocal lattice vectors: $(1,0) \cdot 2\pi/a$ for $\phi = 0°$, and $(1,1) \cdot 2\pi/a$ for $\phi = 45°$. (In fact, it is possible to calculate, to first order, the locations of the gaps using the dynamic structure factor $S(\mathbf{k}, \omega)$ obtained from the projection of the superspace

lattice.[71]) For intermediate angles, a number of smaller gaps open and then close. If we were able to show the spectrum with higher resolution, we would expect to see increasing numbers of these smaller gaps opening, leading to the well-known fractal structure that arises e.g. for the Fibonacci crystal.

### 1.3.4. *Smooth superspace structures*

Thus far, we have examined dielectric structures in which the permittivity function attains only two values: such structures are the most realistic for fabrication. However, for theoretical purposes it can be enlightening to consider cases in which the sharp boundaries are smoothed out, in order to restrict the number of Fourier components appearing in the structure factor (for example, this is useful for examining the origin of bandgaps in one-dimensional photonic crystals[60]). The superspace construction allows one to consider a conceptually interesting class of structures, involving *superspace* dielectrics described by smooth functions. In particular, we examine the case in which the superspace dielectric function is given by:

$$\varepsilon(x,y) = 1 + 4e^{-(\sin^2(x) + \sin^2(y))} . \tag{1.4}$$
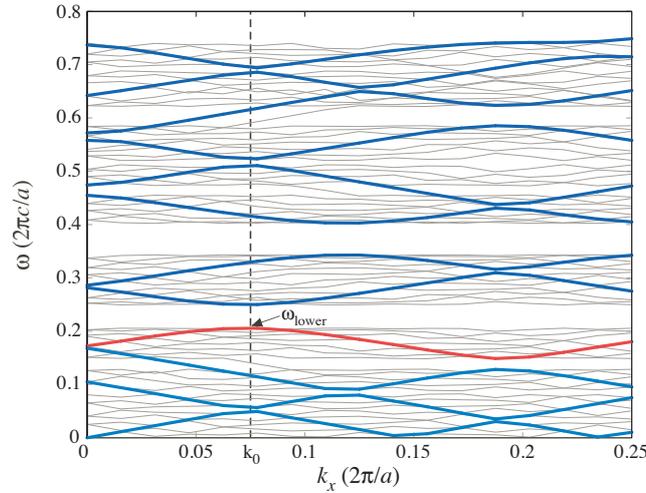


**Figure 1.14.** Bandstructure for the smooth superspace structure $\varepsilon(x,y) = 1 + 4e^{-(\sin^2(x)+\sin^2(y))}$ at two resolutions: thick lines denote 6 pixels / $a$, and thin lines denote 32 pixels / $a$. We will demonstrate that the bandstructure for this dielectric converges *exponentially* in resolution by examining the frequency $\omega_{\text{lower}}$, indicated on the figure, which is at a relative maximum of the lower band edge (colored red) at a fixed $k_0 \approx 0.75(2\pi/a)$.

The Fourier components of the previous square dielectric scales as $\varepsilon_{\mathbf{G}} \sim |\mathbf{G}|^{-1}$; however, the Fourier transform of Eq. (1.4) converges *exponentially* for large $|\mathbf{G}|$. This implies[72] that the frequencies at the bandgaps will also converge exponentially with the resolution (i.e., the number of reciprocal vectors $\mathbf{G}$ retained in the computation). The bandstructure for the smooth dielectric is shown in Fig. 1.14.; two resolution are shown, resolution 6 and 32. In order to confirm the exponential convergence of this bandstructure, we examine the value $\omega_{\text{lower}}(k_0)$ shown

in Fig. 1.14., which is the extremal value of the band depicted in red. We fix the value of $k_x = k_0 = 0.075415(2\pi/a)$ and increase the resolution, examining the value of $\omega$ at the bottom of this bandgap. The results, shown in Fig. 1.15., confirm the exponential convergence with resolution. This is an interesting property, which may be useful for structural optimization, where the exponential convergence allows for efficient optimization with only a few number of grid parameters.
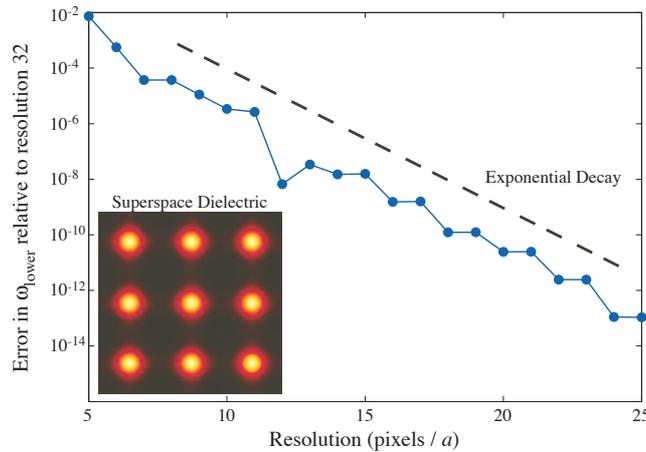


**Figure 1.15.** Demonstration of exponential convergence with resolution of a smooth superspace structure. A plot of the error in $\omega_{\text{lower}}$ from Fig. 1.14. (relative to resolution 32) shows exponential convergence. The superspace dielectric structure, given by Eq. (1.4), is shown in the inset.

### 1.3.5. *Optimization of one-dimensional smoothed structures*

Previously, we examined the effect of varying the cut angle on the bandstructure. In this section, we examine the superspace structures that give the largest fractional photonic bandgaps, for a fixed cut angle. The superspace construction is very convenient for this purpose because the entire structure resides within one compact unit cell. We employ a technique called topology optimization,[73–76] specifically by using the method of moving asymptotes (MMA) algorithm.[77,78] Here, each pixel $\varepsilon_i$ of the dielectric is treated as a free parameter, and allowed to vary freely between the values $\varepsilon_{\min} = 1$ and $\varepsilon_{\max} = 10$. We start with the same geometry as Fig. 1.1. (although now with a higher index contrast). Above, we saw that smoothed superspace structures require much lower discretization to reach convergence. However, smoothed structures also have another useful property: a lack of local minima for optimization. To obtain a smooth structure, we convolve the initial square of Fig. 1.1. with a Gaussian kernel with standard deviation $\sigma = 0.25$. The resulting smoothed superspace structure is shown on the top left of Fig. 1.16., and its bandstructure is shown in the center. A continuous structural change will change the bandstructure continuously as well, therefore we can uniquely track
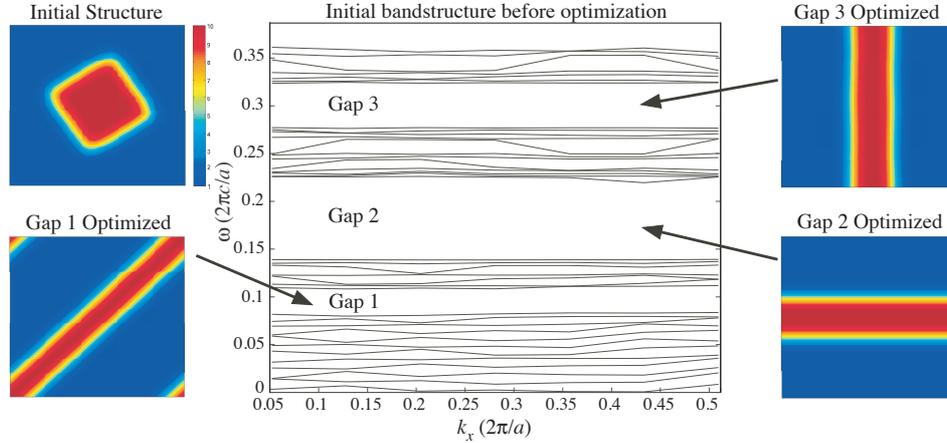
**Figure 1.16.**   Optimization of the fractional bandgap for a 1d quasicrystal: starting with a smoothed version of the Fibonacci structure (top left), which has the indicated bandstructure, we allow every pixel to be a free parameter, ranging from $1 \leq \varepsilon \leq 10$. Even though the cut angle is $\tan \phi = \tau$, the three structures shown are actually *periodic*. After optimization, all structures exhibit an approximately 67% fractional bandgap, which is the same as an optimized 1d photonic crystal with the same smoothing parameters.

the evolution of an individual bandgap through the optimization.[b] We will separately optimize the bandgaps labeled 1, 2, and 3 in this figure, using a resolution of 32 pixels per *a* (at this resolution, these bandgaps have lower edge 13, 20, and 32, respectively), although lower resolutions provide similar results.

The results of the topology optimization are shown in the different panels of Fig. 1.16.. What is interesting is that, despite the aperiodic nature of the initial structure, the optimized structures are *periodic*, regardless of the cut angle. The optimization of different bandgaps results in different periodic structures, and is closely reminiscent of Fig. 1.9.. In fact, this is another manifestation of the 1d structure inheriting its behavior from the 2d superspace: the band edge states of Fig. 1.9. have a dominant wavevector that corresponds to a low-order superspace reciprocal vector; we expect the optimized structure to strongly couple to this reciprocal vector. For all structures, the optimized gap-midgap ratio is approximately 67%. Intuitively, we expect that this result should correspond to the optimized gap-midgap ratio for a purely 1d periodic structure. Using the same smoothing parameters and applying the topology optimization to the first bandgap of a 1d photonic crystal, we again get a 67% gap-midgap ratio, confirming this expectation; furthermore, the optimized 1d structure corresponds exactly to a quarter-wave stack (convolved with a $\sigma = 0.25$ Gaussian).

---

[b]This is not strictly true when spurious modes are encountered, however for this particular situation they are absent.

## 1.4.  Two-dimensional results

The superspace approach can also be applied to higher-dimensional quasicrystal structures. Here, we examine this possibility by focusing on two-dimensional quasicrystals that can be represented by a four-dimensional superspace. The implementation in a planewave-expansion method is fairly simple: unlike finite-difference methods, it is straightforward to extend a planewave-expansion method to higher dimensions. This is because the process of differentiation, which for finite-difference methods requires knowledge of the lattice structure, is simply achieved by multiplying by $\mathbf{k} + \mathbf{G}$ in a planewave basis. The actual quasicrystal structure is represented by three matrices. $\overleftrightarrow{R}_{\text{Super}}$ defines the lattice structure in the superspace; the rows of this matrix represent the basis vectors; $\overleftrightarrow{R}_X$ defines the physical space - the rows of this matrix represent the superspace basis vectors; finally, $\overleftrightarrow{R}_Y$ defines the subspace perpendicular to the physical space. As with the one-dimensional quasicrystals of the previous section, the superspace dielectric is the Cartesian product of a "physical" profile and a "perpendicular" profile. Here, we will take the physical profile to be a circle of radius $r$. The perpendicular profile, defined by cut-and-project, is the projection of the convex hull (i.e., the Voronoi cell[34,35]) of the superspace basis vectors onto the perpendicular space; that is, the convex hull of the set $\overleftrightarrow{R}_Y^T \overleftrightarrow{R}_{\text{Super}}$. We compute the convex hull using Qhull,[79] a freely-available software program.

### 1.4.1.  *Octagonal Quasicrystals*
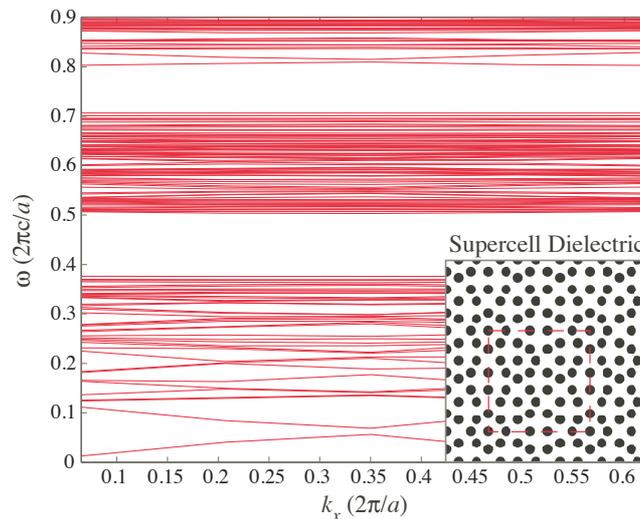


**Figure 1.17.**   Bandstructure for a 3/2 supercell approximate to the octagonal PQC of high dielectric rods. The real-space structure is shown in the inset, with a unit cell marked by the dashed red box.

The two-dimensional octagonal quasicrystal is constructed from slicing four-

dimensional Cartesian space. The Fourier spectrum of the octagonal lattice has 8-fold rotational symmetry.[3,36] Since the superspace lattice is Cartesian, the matrix $\overleftrightarrow{R}_{\text{Super}}$ is simply the $4 \times 4$ identity matrix. The other two matrices are:[36]

$$\overleftrightarrow{R}_X = \begin{pmatrix} \frac{1}{\sqrt{2}} & \frac{1}{2} & 0 & -\frac{1}{2} \\ 0 & \frac{1}{2} & \frac{1}{\sqrt{2}} & 0 \end{pmatrix} \tag{1.5}$$

and

$$\overleftrightarrow{R}_Y = \begin{pmatrix} \frac{1}{\sqrt{2}} & \frac{1}{2} & 0 & \frac{1}{2} \\ 0 & -\frac{1}{2} & \frac{1}{\sqrt{2}} & -\frac{1}{2} \end{pmatrix}. \tag{1.6}$$

We first compute a bandstructure using a supercell with a rational approximate; the dielectric for the rational approximate can be constructed by following the same cut-and-project procedure as for the superspace, with the modification that $\sqrt{2}$ for $\overleftrightarrow{R}_X$ is replaced with $p/q$ for integer $p$ and $q$. The resulting $\overleftrightarrow{R}_Y$ will no longer be orthogonal to the physical subspace; rather, it is constructed from the rows of $\overleftrightarrow{R}_X$ using Gram-Schmidt orthogonalization. The supercell spectrum is shown in Fig. 1.17., where a $p = 3$, $q = 2$ rational approximate has been used (the 2d dielectric function has period $\approx 4.12$, and is shown in Fig. 1.17.[Inset]). We see the presence of two large bandgaps (the gap-midgap ratios are $\approx 30\%$ for the lower gap and $\approx 15\%$ for the upper gap).

Unfortunately, computational limitations restrict the resolution that can be applied to a four-dimensional planewave expansion; this is because for $N$ pixels per $a$ the computational resources (both space and time) scale as $N^6$. Therefore, it is difficult to reach high enough resolution so that the method for eliminating spurious modes (discussed above) becomes strictly valid. A superspace bandstructure computation at resolution $a/10$ is shown in Fig. 1.18. as a mode-density plot. We identify both of the major bandgaps corresponding to the supercell bandstructure of Fig. 1.17.. However, due to the low resolution we can only resolve the lower edge of the first bandgap to high accuracy. It remains to go to a sufficiently high resolution to fully reproduce this bandstructure using a superspace computation.

## 1.5. Concluding Remarks

In this chapter, we reviewed both superspace and supercell methods for computing PQC spectra, both of which offer unique advantages. On the one hand, the supercell method allows one to control the resolution and supercell approximation independently of one another, and this flexibility can be exploited to obtain reasonable accuracy for moderately sized (even discontinuous) structures. On the other hand, supercell techniques allow one to capture the entire infinite aperiodic quasicrystal in a single finite computational cell, albeit at only a finite resolution. In this way, the single convergence parameter of spatial resolution replaces the combination of resolution and supercell size in traditional supercell calculations, in some sense uniformly sampling the infinite quasicrystal. In addition to yielding exponential convergence with respect to resolution for smooth structures (and
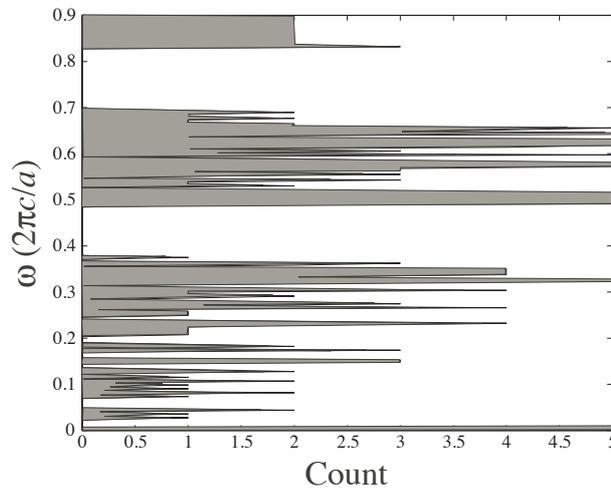
**Figure 1.18.**   Mode density plot for the super*space* octagonal structure, with the same structural parameters as Fig. 1.17., for a resolution of 10 pixels per *a*. At this resolution, the bandgaps are not fully resolved to high accuracy.

in principle high-order convergence for discontinuous structures using high-order finite-element methods), the supercell method offers a unique way to visualize and understand the resulting PQC spectra.

### References

1. M. Kohmoto, B. Sutherland, and K. Iguchi, Localization in optics: Quasiperiodic media, *Phys. Rev. Lett.* **58**(23), 2436–2438, (1987).
2. W. Gellermann, M. Kohmoto, B. Sutherland, and P. Taylor, Localization of light waves in fibonacci dielectric multilayers, *Phys. Rev. Lett.* **72**(5), 633–636, (1994).
3. Y. S. Chan and Z. Y. Liu, Photonic band gaps in two dimensional photonic quasicrystals, *Phys. Rev. Lett.* **80**(5), 956–959, (1998).
4. S. S. M. Cheng, L.-M. Li, C. T. Chan, and Z. Q. Zhang, Defect and tranasmission properties of two-dimensional quasiperiodic photonic band-gap systems, *Phys. Rev. B*. **59**(6), 4091–4099, (1999).
5. C. Jin, B. Cheng, B. Man, Z. Lo, and D. Zhang, Band gap and wave guiding effect in a quasiperiodic photonic crystal, *Appl. Phys. Lett.* **75**(13), 1848–1850, (1999).
6. C. Jin, B. Cheng, B. Man, Z. Li, and D. Zhang, Two-dimensional dodecagonal and decagonal quasiperiodic photonic crystals in the microwave region, *Phys. Rev. B*. **61**, 10762–10767, (2000).
7. M. E. Zoorob, M. D. B. Charlton, G. J. Parker, J. J. Baumberg, and M. C. Netti, Complete and absolute photonic bandgaps in highly symmetric photonic quasicrystals embedded in low regractive index materials, *Mat. Science and Eng.* **74**, 168–174, (2000).
8. M. E. Zoorob, M. D. Charlton, G. J. Parker, J. J. Baumberg, and M. C. Netti, Complete photonic bandgaps in 12-fold symmetric quasicrystals, *Nature*. **404**, 740–743, (2000).
9. L. Dal Negro, C. J. Oton, Z. Gaburro, L. Pavesi, P. Johnson, A. Lagendijk, R. Righini, M. Colocci, and D. Wiersma, Light transport through the band-edge states of Fibonacci quasicrystals, *Phys. Rev. Lett.* **90**(5), 055501, (2003).
10. Y. Wang, C. Bingying, and D. Zhang, The density of states in quasiperiodic photonic crystals, *J. Phys.: Cond. Mat.* **15**, 7675–7680, (2003).
11. P. Xie, Z.-Q. Zhang, and X. Zhang, Gap solitons and soliton trains in finite-sized two-

dimensional periodic and quasiperiodic photonic crystals, *Phys. Rev. E.* **67**, 026607, (2003).

12. M. Notomi, H. Suzuki, T. Tamamura, and K. Edagawa, Lasing action due to the two-dimensional quasiperiodicity of photonic qyasicrystals with Penrose lattice, *Phys. Rev. Lett.* **92**(12), 123906, (2004).

13. D. V. A., S. Enoch, G. Tayeb, V. Pierro, V. Galdi, and F. Capolino, Bang gap formation and multiple scattering in photonic quasicrystals with Penrose-type lattice, *Phys. Rev. Lett.* **94**, 183903, (2005).

14. Z. Feng, X. Zhang, Y. Wang, Z.-Y. Li, B. Cheng, and D.-Z. Zhang, Negative refraction and imaging using 12-fold-symmetry quasicrystals, *Phys. Rev. Lett.* **94**(24), 247402, (2005).

15. S.-K. Kim, J.-H. Lee, S.-H. Kim, I.-K. Hwang, and Y.-H. Lee, Photonic quasicrystal single-cell cavity mode, *Appl. Phys. Lett.* **86**, 031101, (2005).

16. R. Lifshitz, A. Arie, and A. Bahabad, Photonic quasicrystals for nonlinear optical frequency conversion, *Phys. Rev. Lett.* **95**, 133901, (2005).

17. J. Romero-Vivas, D. N. Chigrin, A. V. Lavrinenko, and C. M. Sotomayor Torres, Photonic quasicrystals for application in WDM systems, *Phys. Stat. Sol.* **202**(6), 997–1001, (2005).

18. D. S. Wiersma, R. Sapienza, S. Mujumdar, M. Colocci, M. Ghulinyan, and L. Pavesi, Optics of nanostructured dielectrics, *J. Opt. A: Pure and Appl. Opt.* **7**, S190–S197, (2005).

19. A. Della Villa, S. Enoch, G. Tayeb, V. Pierro, and V. Galdi, Localized modes in photonic quasicrystals with Penrose-type lattice, *Opt. Express.* **14**(21), 10021–10027, (2006).

20. B. Freedman, G. Bartal, M. Segev, R. Lifshitz, D. N. Christodoulides, and J. W. Fleischer, Wave and defect dynamics in nonlinear photonic quasicrystals, *Nature.* **440**, 1166–1169 (April, 2006).

21. R. C. Gauthier and K. Mnaymneh, FDTD analysis of 12-fold photonic quasicrystal central pattern localized states, *Opt. Comm.* **264**, 78–88, (2006).

22. G. J. Parker, M. D. B. Charlton, M. E. Zoorob, J. J. Baumberg, M. C. Netti, and T. Lee, Highly engineered mesoporous structures for optical processing, *Phil. Trans. Soc. A.* **364**, 189–199, (2006).

23. Z. S. Zhang, B. Zhang, J. Xu, Z. J. Yang, Z. X. Qin, T. J. Yu, and D. P. Yu, Effects of symmetry of GaN-based two-dimensional photonic crystal with quasicrystal lattices on enhancement of surface light extraction, *Appl. Phys. Lett.* **88**, 171103, (2006).

24. J. Y. Zhang, H. L. Tam, W. H. Wong, Y. B. Pun, J. B. Xia, and K. W. Cheah, Isotropic photonic bandgap in Penrose textured metallic microcavity, *Sol. State Comm.* **138**, 247–249, (2006).

25. K. Mnaymneh and R. C. Gauthier, Mode localization and band-gap formation in defect-free photonic quasicrystals, *Opt. Express.* **15**(8), 5089–5099, (2007).

26. M. C. Rechtsman, H.-C. Jeong, P. M. Chaikin, S. Torquato, and P. J. Steinhardt, Optimized structures for photonic quasicrystals, *Phys. Rev. Lett.* **101**, 073902, (2008).

27. M. E. Pollard and G. J. Parker, Low-contrast bandgaps of a planar parabolic spiral lattice, *Opt. Express.* **34**(18), 2805–2807, (2009).

28. A. N. Poddubny and E. L. Ivchenko, Photonic quasicrystalline and aperiodic structures, *Physica E: Low-dimensional systems and nanostructures.* **42**(7), 1871–1895, (2010).

29. M. A. Kaliteevski, S. Brand, R. A. Abram, T. F. Krauss, P. Millar, and R. De La Rue, Diffraction and transmission of light in low-refractive index Penrose-tiled photonic quasicrystals, *J. Phys: Cond. Mat.* **13**, 10459–10470, (2001).

30. X. Zhang, Z.-Q. Zhang, and C. T. Chan, Absolute photonic band gaps in 12-fold symmetric photonic qusicrystals, *Phys. Rev. B.* **63**, 081105–081108, (2001).

31. M. Hase, H. Miyazaki, M. Egashira, N. Shinya, K. Kojima, and S.-i. Uchida, Photonic band gap and anisotropic structures in transmission spectra of two-dimensional five-fold and eightfold symmetric quasiperiodic photonic crystals, *Phys. Rev. B.* **66**, 214205–214212, (2002).

32. M. Maldovan and E. L. Thomas, Diamond-structured photonic crystals, *Nature Materials.* **3**, 593–600, (2004).

33. A. W. Rodriguez, A. P. McCauley, Y. Avniel, and S. G. Johnson, Computation and visualization of photonic quasicrystal spectra via blochs theorem, *Phys. Rev. B*. **77**(10), 104201, (2008).

34. C. Janot, *Quasicrystals*. (Clarendon Press, 1992).

35. M. Baake, *A Guide to Mathematical Quasicrystals*, In eds. J. B. Suck, M. Schreiber, and P. Haussler, *Quasicrystals*, chapter 2. Springer, (2004).

36. K. Wang, S. David, A. Chelnokov, and J. M. Lourtioz, Photonic band gaps in quasicrystal-related approximant structures, *J. Mod. Opt.* **50**(13), 2095–2105, (2003).

37. W. Man, M. Megens, P. J. Steinhardt, and P. M. Chaikin, Experimental measurement of the photonic crystal properties of icosahedral quasicrystals, *Nature*. **436**, 993–996 (August, 2005).

38. A. Ledermann, L. Cademartiri, M. Hermatschweiler, C. Tonninelli, G. A. Ozin, D. S. Weirsma, M. Wegener, and G. V. Freymann, Three-dimensional silicon inverse photonic quasicrystals for infrared wavelengths, *Nature Mat.* **5**, 942–945 (December, 2006).

39. C. de Lange and T. Janssen, Electrons in incommensurate crystals: Spectrum and localization, *Phys. Rev. B*. **28**(1), 195–209, (1983).

40. J. P. Lu and J. L. Birman, Electronic structure of a quasiperiodic system, *Phys. Rev. B*. **36** (8), 4471–4474, (1987).

41. C. Godreche, Indexing the diffraction spectrum of a non-pisot self-similar structure, *Phys. Rev. B*. **45**(1), 176–185, (1992).

42. X. Q. Huang, S. S. Juang, R. W. Peng, and A. Hu, Perfect transmission and self-similar optical transmission spectra in symmetric Fibonacci-class multilayers, *Phys. Rev. B*. **63**, 245104–245112, (2001).

43. R. C. Gauthier and K. Mnaymueh, Photonic band gaps properties of 12-fold quasicrystal determined through fdtd analysis, *Opt. Express*. **13**(6), 1985–1998, (2005).

44. T. D. M. Lee, G. J. Parker, M. E. Zoorob, and M. D. B. Charlton, Design and simulation of highly symmetric photonic quasi-crystals, *Nanotechnology*. **16**(11), 2703–2706, (2005).

45. J. Yin, X. Huang, S. Liu, and S. Hu, Photonic bandgap properties of 8-fold symmetric photonic quasicrystals, *Opt. Comm.* **269**(2), 385–388, (2006).

46. L. Jia, I. Bita, and E. L. Thomas, Photonic density of states of two-dimensional quasicrystalline photonic structures, *Phys. Rev. B*. **61**(16), 10762–10767, (2011).

47. M. A. Kaliteevski, S. Brand, R. A. Abram, T. F. Krauss, R. M. De La Rue, and P. Millar, Two-dimensional penrose-tiled photonic quasicrystals: Diffraction of light and fractal density of modes, *J. Mod. Opt.* **47**, 1771–1778, (2000).

48. A. Della Villa, V. Galdi, F. Capolino, V. Pierro, S. Enoch, and G. Tayeb, A comparative study of representative categories of EGB dielectric quasi-crystals, *IEEE Ant. Wireless Prop. Lett.* **5**, 331–333, (2006).

49. M. Florescu, S. Torquato, and P. J. Steinhardt, Complete band gaps in two-dimensional photonic quasicrystals, *Phys. Rev. B*. **80**, 155112, (2009).

50. W. Steurer and D. Sutter-Widmer, Photonic and phononic quasicrystals, *J. Phys. D*. **40**, R229–R247, (2007).

51. E. S. Zijlstra and T. Janssen, Non-spiky density of states of an icosahedral quasicrystal, *Europhys. Lett.* **52**(5), 578–583, (2000).

52. C. Cohen-Tannoudji, B. Din, and F. Laloë, *Quantum Mechanics*. (Hermann, Paris, 1977).

53. G. Zito, T. P. Rose, E. Di Gennaro, A. Andreone, E. Santamato, and G. Abbate, Bandgap properties of low-index contrast aperiodically ordered photonic quasicrystals, *Micro. Opt. Tech. Lett.* **51**(11), 2732–2737, (2009).

54. W. C. Chew, J. Jian-Ming, E. Michielssen, and S. Jiming, *Fast and Efficient Algorithms in Computational Electromagnetics*. (Artech, Norwood, MA, 2001).

55. L. Dal Negro, M. Stolfi, Y. Yi, J. Michel, X. Duan, L. C. Kimerling, J. LeBlanc, and J. Haavisto, Photon band gap properties and omnidirectional reflectance in si/siO$_2$ thue-morse quasicrystals, *Appl. Phys. Lett.* **84**(25), 5186–5188, (2004).

56. R. Lifshitz, The square fibonacci tiling, *J. of Alloys and Compounds*. **342**, 186–190, (2000).

57. V. Matarazzo, S. D. Nicola, G. Zito, P. Mormile, M. Rippa, J. Zhou, and L. Petti, Spec-

tral characterization of two-dimensional ThueMorse quasicrystals realized with high resolution lithography, *J. Opt.* **13**(1), 015602, (2011).

58. G. H. Hardy and E. M. Wright, *An Introduction to the Theory of Numbers*. (Oxford University Press, Oxford, 1979), 5th edition.

59. W. A. Coppel, *Number Theory: an Introduction to Mathematics*. (Springer, New York, 2009), 2nd edition.

60. J. D. Joannopoulos, R. D. Meade, and J. N. Winn, *Photonic Crystals: Molding the Flow of Light*. (Princeton Univ. Press, 1995).

61. S. G. Johnson and J. D. Joannopoulos, Block-iterative frequency-domain methods for Maxwell's equations in a planewave basis, *Opt. Express*. **8**(3), 173–190, (2001).

62. G. H. Golub and C. F. Van Loan, *Matrix Computations*. (The Johns Hopkins University Press, Baltimore, Maryland, 1996), 3rd edition.

63. G. Bao, L. Cowsar, and W. Masters, Eds., *Mathematical Modeling in Optical Science*, vol. 22, *Frontiers in Applied Mathematics*, chapter 7. SIAM, (2001).

64. I. Gohberg, S. Goldberg, and M. A. Kaashoek, *Basic Classes of Linear Operators*. (Birkhäuser, Basel, 2000).

65. J. Li, D. Zhao, and Z. Liu, Zero-$\bar{n}$ photonic band gap in a quasiperiodic stacking of positive and negative refractive index materials, *Phys. Lett. A*. **332**, 461–468, (2004).

66. A. Farjadpour, D. Roundy, A. Rodriguez, M. Ibanescu, P. Bermel, J. Burr, J. D. Joannopoulos, and S. G. Johnson, Improving accuracy by subpixel smoothing in the finite-difference time domain, *Opt. Lett.* **31**, 2972–2974, (2006).

67. M. Kohmoto, L. P. Kadanoff, and C. Tang, Localization problem in one dimension: Mapping and escape, *Phys. Rev. Lett.* **50**(23), 1870–1872, (1983).

68. S. Ostlund, R. Pandit, D. Rand, H. Scheller, and E. Siggia, One-dimensional Schrödinger equation with an almost periodic potential, *Phys. Rev. Lett.* **50**(23), 1873–1876, (1983).

69. M. Bayinding, E. Cubukcu, I. Bulu, and E. Ozbay, Photonic band gaps and localization in two-dimensional metallic quasicrystals, *Europhys. Lett.* **56**(1), 41–46, (2001).

70. W. Steurer and T. Haibach, *Crystallography of Quasicrystals*, In eds. W. Steurer and T. Haibach, *Physical Properties of Quasicrystals*, chapter 2. Springer, (1999).

71. M. Quilichini, Phonon excitations in quasicrystals, *Reviews of Modern Physics*. **69**(1), 277–314, (1997).

72. J. P. Boyd, *Chebychev and Fourier Spectral Methods*. (Dover, New York, 2001), 2nd edition.

73. M. P. Bendsoe and S. Ole, *Topology Optimization: Theory, Methods, and Applications*. (Springer, Berlin, 2003), 2nd edition.

74. P. I. Borel, A. Harpoth, L. H. Frandsen, M. Kristensen, P. Shi, J. S. Jensen, and O. Sigmund, Topology optimization and fabrication of photonic crystal structures, *Opt. Express*. **12**, 1996, (2004).

75. C. Y. Kao, S. Osher, and E. Yablonovitch, Maximizing band gaps in two-dimensional photonic crystals by using level set methods, *Appl. Phys. B*. **81**, 235, (2005).

76. W. R. Frei, D. A. Tortorelli, and H. T. Johnson, Geometry projection method for optimizing photonic nanostructures, *Opt. Lett.* **32**, 77, (2007).

77. S. G. Johnson. The nlopt nonlinear-optimization package. `http://ab-initio.mit.edu/nlopt`.

78. K. Svanberg, A class of globally convergent optimization methods based on conservative convex separable approximations, *SIAM J. Optim.* **12**, 555, (2002).

79. `http://www.qhull.org`.